Electronic Theses and Dissertations

4-17-2017

Building 3-D Geometry of Retinal Vasculature From Optical Coherence Tomography Volume Scans

Wasi Uddin Ahmed

BUILDING 3-D GEOMETRY OF RETINAL VASCULATURE FROM OPTICAL COHERENCE TOMOGRAPHY VOLUME SCANS

by

Wasi Uddin Ahmed

A Thesis

Submitted in Partial Fulfillment of the

Requirements for the degree of

Master of Science

Major: Electrical and Computer Engineering

The University of Memphis

May 2017

ACKNOWLEDGEMENT

I am extremely grateful to my advisor Dr. Madhusudhanan Balasubramanian, Assistant Professor in the Department of Electrical and Computer Engineering (EECE), At The University of Memphis for his undue encouragement, guidance as well as inspiring me throughout my graduate studies.

I would also like to express my gratitude to my committee members, Dr. Aaron L. Robinson and Dr. Hasan Ali for their support and advice. This study would not have been possible without the graduate teaching assistantship from the EECE department and research assistantship from Dr. Balasubramanian.

The research work presented here was supported in part by research funding from the National Eye Institute, National Institutes of Health grant EY020518 and in part by a startup funding for Dr. Balasubramanian from the Herff College of Engineering, The University of Memphis.

I would like to express my gratitude toward my parents whose generous sacrifices and support made this work possible. Finally, I would like to thank my lab mates and friends for being a part of my graduate studies and for their help.

ABSTRACT

Assessing vascular structure of the retina is useful for diagnosis and management of pathological conditions of the eye such as glaucoma, diabetic retinopathy, vein occlusion and retinal neo-vascularization. Optical coherence tomography (OCT) is an optical imaging technique based on the principle of low-coherence interferometry and can be used to image various ocular structures non-invasively. Ocular structures such as blood vessels and collagen with high optical absorption and/or scattering significantly attenuate OCT light propagation and thus, cast shadows below these highly attenuating locations in OCT a-scans. An improved attenuation compensation procedure is presented to minimize shadows and resolve tissue structure by solving an integral equation with exponential non-linearity that govern OCT light transport in a tissue. *Frangi* filter was used to extract retinal blood vessel network from 2D photographs and 3D OCT scans of the retina. The location and orientation of retinal blood vessels were identified using eigen analysis of the Hessian matrix at each retinal location. Vessels of varying diameters were identified by conducting eigen analysis at multiple scales using scale-space theory. Further, a 3-D geometrical model of the vessel network was extracted from the scale-space analysis. Our methodology was evaluated using 2D photographs of human subjects and 3D OCT volume scans of the retina of porcine eyes. Results demonstrate that the proposed attenuation compensation procedure and retinal vessel extraction from OCT scans using Frangi filter is feasible. Matlab, Python, VolView and VTK software libraries were used for software analysis and visualization.

TABLE OF CONTENTS

LIST OF FIGURES

1. INTRODUCTION

Assessing vascular structure of the eye is useful for diagnosis and management of various ocular diseases such as glaucoma, ocular manifestations, retinal abnormalities and hemorrhages, vein occlusion, neo-vascularization diseases. Documenting the position of blood vessels is also useful for specifying the relative geometric locations of the optic disk, lesions and fovea.

Abnormalities in the appearance of the blood vessel, its diameter, color and tortuosity are useful indicators of several ocular conditions. Neovascular condition in diabetic retinopathy causes weaker new vessel growths that debilitates and leak blood and fluid into retina. Retinal blood vessel damage is also common due to hypertension. Central retinal vein occlusion is another vascular condition in which blood starts to leak from blood vessels causing damage to the retina.

Ocular structures can be non-invasively imaged using optical imaging instruments such as photography, confocal scanning laser microscope, and optical coherence tomography (OCT). Ocular structures with high optical absorption and/or scattering may significantly attenuate the OCT signal propagation beyond these highly attenuating locations in the eye. For complete estimate of the tissue characteristics, it is useful to recover the tissue resolution below these attenuating locations.

In this thesis, we present a modified attenuation compensation procedure that is adaptive to the tissue being imaged to compensate for OCT signal attenuation near highly attenuating structures such as blood vessels. The attenuation compensation procedure presented in this thesis is a modification of the adaptive compensation technique developed by Hughes and Duck [1] and adapted for applications in OCT by Girard M, et al [2]. Further, we present applications of *Frangi* filter to enhance and extract vascular structure from the optical images of the retina.

2. BACKGROUND

2.1. ANATOMY OF EYE:

Lights enter the eye through the cornea, passes through the pupil and becomes focused on the retinal layers by the lens. The iris controls how much light reaches the retinal layers. The retina consists of 10 distinct layers. There are two types of photoreceptor cells namely rods and cones. Cones are less sensitive to light than rods. Rods are insensitive to color and are useful for low light vision. On the other hand, cones provide daylight color vision. Light crosses neuronal layers to reach the photoreceptors because photoreceptors lie underneath the neuronal cells and close to retinal pigment epithelium (RPE) in retina. [3-5]. Fibers of the neuronal cells help to guide light to photoreceptors. RPE also absorbs light and thus prevents light backscatter onto the photoreceptors. (Figure 2.1)

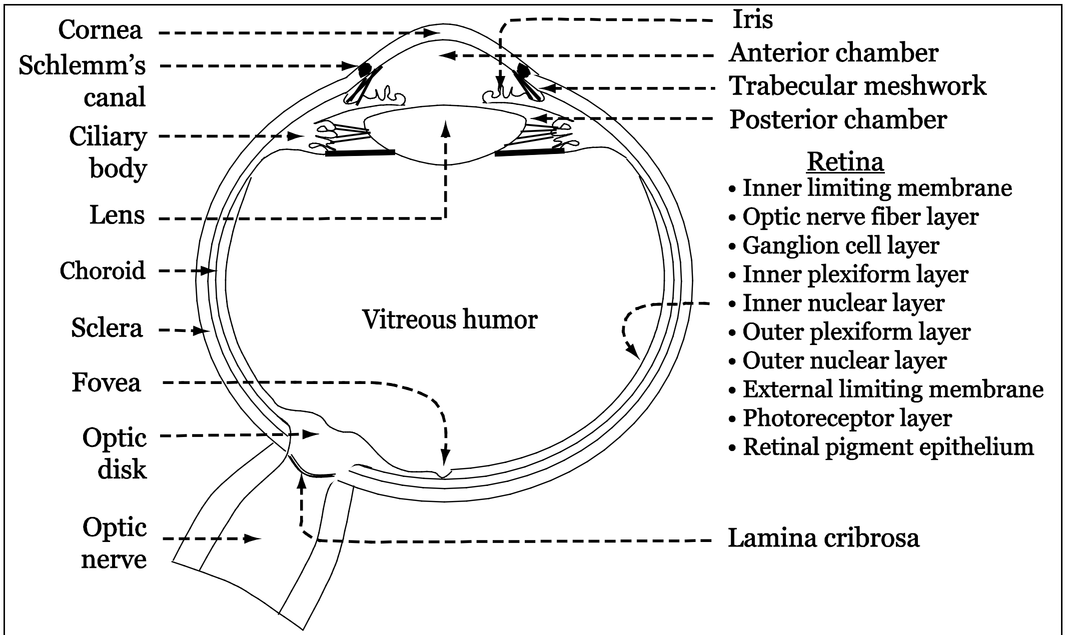

Figure 2.1: Human Eye Schema

Bipolar and horizontal cells of nuclear layer combine chemical responses of photoreceptors and pass the responses to ganglion cells of ganglion cell layers. Ganglion cells convert chemical responses to electric responses. Axons of ganglion cells group together to form the optic nerve and carry electric signals to The visual cortex of the brain for image representation. Optic nerve fibers run parallel and exit the eye at optic disc. [6] An optic nerve exits the eye through scleral canal. A healthy human eye has more than one million optic nerve head.

Functionality of the eye heavily depends upon maintaining eye shapes and convex shape of cornea. Maintaining eye shapes and convex shape of cornea controlled by intraocular pressure (IOP), in the range of 10 to 21 mmHg above atmospheric layer. IOP is maintained by aqueous humor production and outflow. Aqueous humor is a clear liquid which helps to distribute nutrition and immune responses to lens, iris in case of infections. Aqueous humor also helps to clear metabolic wastes. [7]

2.2. RETINAL VASCULAR STRUCTURE OF HUMAN EYE:

Gas exchange in the lungs oxygenates the blood. Oxygenated blood from the lungs reaches the left atrium of the heart through pulmonary veins. The left atrium relaxes and pushes the blood to left ventricle. The oxygenated blood then goes to aorta. Arteries carry oxygenated blood to different parts of the body and they further branch into capillaries to reach different organs of the body. Blood ends become deoxygenated and blood Capillaries are mixed with thicker blood vessels called veins. Veins carry deoxygenated blood to right side of the heart into the pulmonary artery that carries deoxygenated blood to lungs for oxygenation.

Fig. 2.2 shows a schematic representation of the vascular structure and blood supply in the retina. Branches of the ophthalmic artery namely the central retinal artery and ciliary retinal trunks provide blood supply to the eye. The central retinal artery mainly provides blood supply to retina; central retinal artery enters through the optic nerve head. In the optic nerve, artery divides in two trunks and each of these trunks separate to form superior and inferior nasal trunks. They provide blood supply to four quadrants of the retina.

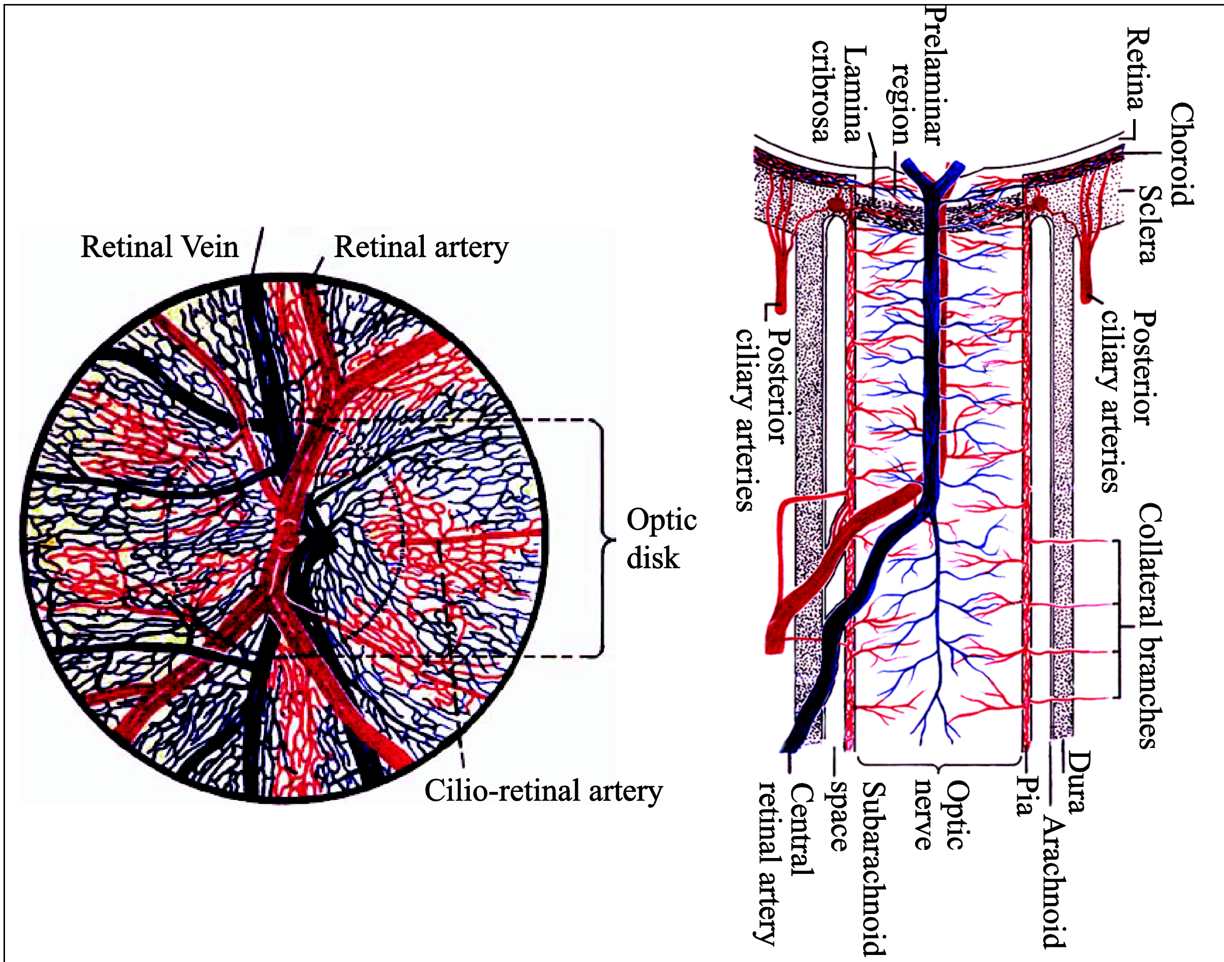

(a) Schematic representation of retinal vasculature in the optic nerve head region

(b) Schematic representation of blood supply to the optic nerve

Figure 2.2: Schematic representation of retinal vasculature and retinal blood supply to the optic nerve head. Source: Andand-Apte B, et al [8]

The retinal arterial system in the human eye does not communicate with other arterial systems. For this reason, blood supply in each quadrant comes from dedicated retinal artery and vein. If blood supply faces any blockage, then it is called infarction.. A larger artery extends within the retina and moves towards the periphery and the larger artery divides into vessels with smaller diameters until they reach *ora serrata*. From there the blood supply returns to the venous drainage system. From retinal arteries and veins, arterioles and venules form a capillary network in the inner retina. The central retinal vessels branch into two capillary layers and feed the ganglion cell layer and the inner nuclear layer. There are no blood supply from the central retinal artery to the photoreceptor layer. Choriocapillaris provide blood supply to photoreceptors.

The rate of retinal blood circulation is about 1.6-1.7 ml/g of retina where mean circulation time is 4.7s. Rate of blood flowing in retinal vessels is comparatively lower than that of the choroidal vasculature. [8]

2.3. Optical Coherence Tomography

Optical coherence tomography is based on the principle of low coherence interferometry and is useful for imaging the internal microstructure of living tissue at a high axial resolution (~3 nm). [9-12]. The principle design of OCT is similar to that of optical coherence-domain reflectometry (OCDR), a one-dimensional (1-D) optical ranging technique. [13, 14] with applications in assessing fiber optic cables and network components, imaging ocular structures [15-17] and other living tissues. [18, 19] OCT has optical sectioning ability which differs from the conventional bright field and confocal microscope. Using OCT, it is possible to achieve imaging depth exceeding 2 cm in transparent tissues like blood vessels and other structures of eye. [20-24].

OCT is based on the principle of measuring echo time delay of a light backscattered or back reflected from a specimen and the intensity of backscatter similar to ultrasound. Because the speed of light is very high, it is not possible to directly measure the echo time delay. Instead, OCT uses the principle of comparing the echo from a known distance (reference) with that of echoes coming from multiple depths in a specimen based on how they interfere. The echoes interfere either constructively or destructively based on the time delay τ of echo from the sample and is captured using an interferometer. With $E_{Ref}(t)$ as the electric field corresponding to the reference beam and $E_{Spec}(t + \tau)$ as the electric field corresponding to the beam from the sample arm, their interference is $E_{Ref}(t) + E_{Spec}(t + \tau)$. Since, intensity of light is proportional to square of the electric field, intensity of the interferogram is proportional to the correlation or *temporal coherence function* $G(\tau) = E_{Ref}(t) * E_{Spec}(t + \tau)$ which measures the degree of correlation between the reference beam and the beam from the sample.

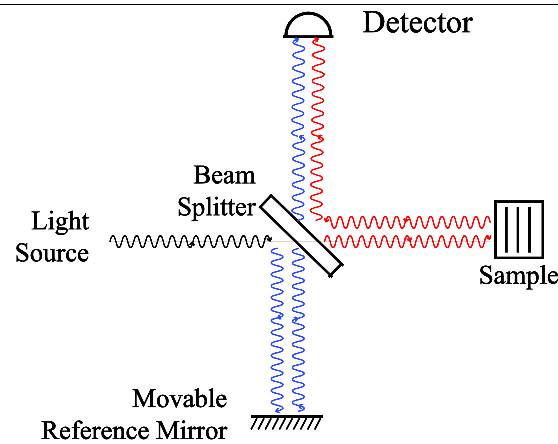

Figure 2.3: Schematic diagram of a Michelson interferometer with a movable sample arm

The threshold of the delay τ_c for which the coherence function drops below a critical value is known as the *coherence time*. Using coherence time, the *coherence length* of the light source is defined as $l_c = c\,\tau_c$, where c is the speed of light. Coherence of a light source is defined based on its coherence length. [25]

OCT is based on a low coherence interferometer such as the Michelson interferometer whose schematic diagram is shown in Fig. 2.3. A beam splitter evenly divides a low coherence light. One of the beams travel along a reference optical arm with a movable reference mirror, and the second beam travels along the sample arm with the sample to be imaged. Light wave reflected by the reference mirror and the backscattered / back reflected light by the sample reach the beam splitter where they interfere. From the interference signal, the detector captures an interferogram. The difference between the distance light travels along the reference arm and the beam travels along the sample arm is known as the optical path difference (OPD) of the interferometer.

In a fiber optic OCT system, low coherence light source is connected to a fiber optic coupler that divides the optical power evenly into the reference and sample arms**.** [26] The fiber optic coupler also collects the reflected light from the mirror in the reference arm and the sample in the sample arm causing them to interfere. A photodetector detector records the *interferogram* (intensity of interference) for various positions of the reference mirror. From the echo time delay at each mirror position, the specimen depth is resolved and reflectivity of the specimen at the corresponding depth is given by the intensity of the interference due to the corresponding mirror position in the reference arm. Thus, the interferometer records the intensity of backscatter proportional to the absorption and backscattering characteristics at a given depth vs. the sample depth (calculated from the echo time delay). This is known as an *a-scan* given by the envelope of the interference signal recorded. By scanning in transverse direction using a scanning mechanism, two dimensional *b-scans* and *volume scans* of the specimen are generated. This is the basic operational principle of a time domain OCT (TD-OCT).

2.3.1 Spectral Domain Optical Coherence Tomography (SD-OCT):

SD-OCT uses a continuous wave, low coherence broadband light source for imaging. Instead of moving the reference mirror to resolve deeper tissue structure as in the TD-OCT, the reference arm length is fixed in place. Instead of using a photodetector, a spectrometer captures a full interference spectrum modulated by interferences between backscattered light from various depths in the specimen and a beam from the fixed reference arm. [27]. Intensity of backscatter and echo time delay from individual tissue locations are obtained by inverse Fourier transform of the individual wavelengths in the interference spectrum.

Fig. 2.4 shows an example a-scan, b-scan and volume scan of the optic nerve head of a porcine eye acquired using a commercial SD-OCT (Spectralis, Heidelberg Engineering, GmbH).

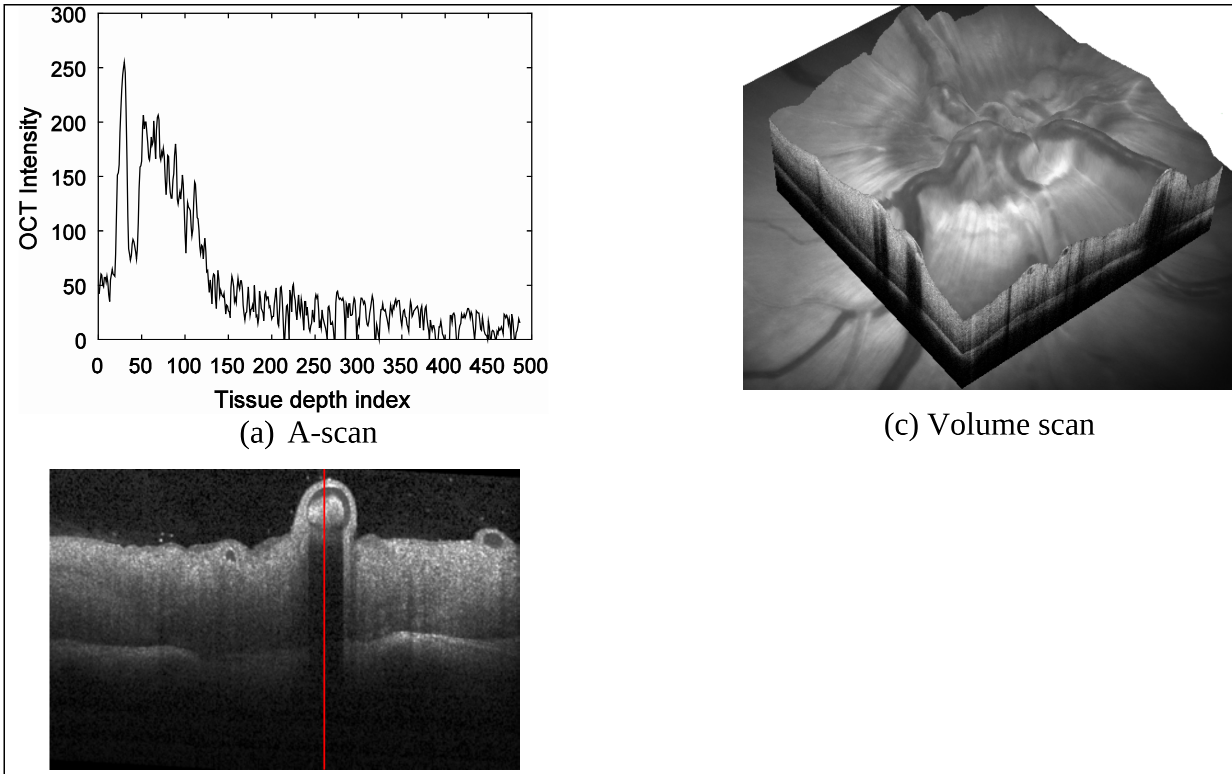

(a) A-scan

(c) Volume scan

(b) B-scan

Figure 2.4: Example spectral domain optical coherence tomography (SD-OCT) scan of the optic nerve head of a porcine eye. A-scan (a) represents the backscatter as a function of the tissue depth. B-scan (b) is comprised of multiple of a-scans and the volume scan (c) is comprised of multiple b-scans by scanning in the transverse direction.

3. LITERATURE REVIEW

Assessing vascular structure is an important diagnostic and disease management strategy in many pathologies. Numerous research literature exists on the topic of automated vessel extraction from various medical imaging modalities ranging from ultrasound, optical imaging to magnetic resonance imaging. For vascular structure assessment using OCT, it is essential to compensate for OCT signal attenuation due to structures such as blood vessels with high optical absorption and/or scattering.

For extracting blood vessels network from the optical images of the retina, it is important to understand the appearance of the optic disk, fovea, and blood vessels in optical images [28, 29]. In 1989, Chaudhuri et al. developed a two-dimensional matched filter to detect retinal blood vessels from fundus photographs using a Gaussian matched filter [30]. In blood vessel detection, one of the main challenges is edge detection, and it is also difficult to differentiate from other vascular structures. For edge detection, quantitative design and performance evaluation techniques have been used which actually works for sharp edges but does not work well when noise is present in the images. [31] Gray scale morphological operations have been also used for edge detection which works better than quantitative design and performance evaluation and work mostly in the presence of salt-and-pepper noise [32] Another well-known method for reducing noise is convolving original image with two dimensional Gaussian filter[33, 34]. Using the spatial intensity changes in the retinal fundus images, edge detection techniques can also be used to identify blood vessels through intensity changes [35]. For vessel tracking, unsupervised fuzzy algorithm has been also used. This method can provide an initial vessel structures and vessel profile for further processing. For detection of blood vessel measurement, fuzzy C-means clustering algorithm is used with properly preprocessed data. [36]

Three-dimensional vessel observed through computed tomography angiography has been extracted through several adaptive steps namely thresholding, region growing, deformable models and multiresolution model based operators [37]. Non-linear fitting technique has also been used for vessel tracking in retinal images. [38] A neural network approach for vessel detection was based approach with 7-D vector composed of gray-level and moment invariants-based features [39]. Matched filter response is widely used for blood vessel detection in retinal images. But matched filter responses also contained few non-vessel edges in addition to the blood vessel measurements. [40-45]. Therefore, first order derivative of Gaussian filter is utilized to get the edges of blood vessels. Differential filtering and morphological processing have been utilized for identifying morphology, diameter, centerlines and branching of blood vessel [46, 47]. For vessel edge detection, sobel method [48], gradient operator [49], directional matched low-pass differentiator template [50] and optimized Canny's detector [51] were proposed. Other methods such as blurred half-elliptical vessel [40], simple rectangular vessel [52] have also been proposed for blood vessels shape detection, though there are difficulties with these techniques.

Vessel measurement is difficult due to several factors such as lower vessel-tissue contrast, tissue characteristics, light source, and modulation of transfer function. Second order Gaussian filter are also suitable for vessel detection by detecting edges and vessel diameters. [53] Kalman filter and extended kalman filter is also very popular for automated vessel tracking which is used after getting estimation from matched filter but it faces challenges in the locations of vessel branching. [54, 55]. In vessel detection, one of the main problems is overlapping non-vascular structures and small vessels with low contrast. Therefore, vessel enhancement can improve small vessels with low contrast condition along with overlapping structures. There are several approaches for vessel enhancement. Some work at fixed scale and some work at multi scale approaches. [56-58] Fixed scale approaches face some problems for vessel detection where multiscale approach was found more efficient for vessel tracking. Multiscale approaches include cores [59], steerable filters [60, 61] and accessing local variables by calculating eigen values and eigen vectors of Hessian matrix. [62, 63]

OCT with its high axial and transverse resolution is a promising technique for non-invasive imaging and assessment of retinal vascular structure. [64-67] Low coherent light propagating through samples is attenuated due to scattering and absorption. Blood vessels also significantly attenuate optical signal and therefore cast shadows below these high attenuating regions.

Attenuation coefficient represents the degree of loss of coherent light intensity due to absorption and/or scattering. [68] Depth resolved attenuation coefficient estimates of the sample may also be useful for enhanced visualization of the retinal structures. [69]

Other previous approaches to improving OCT image quality include Lucy-Richardson deconvolution algorithm [70]; improving attenuation coefficient estimates from b-scans based on automated estimates of confocal functions parameters of OCT image [71]; and quantitative measurement of attenuation coefficients of weakly scattering tissue. [72]

Backscatter estimation is also an indirect approach to improve b-scan image quality as well as to estimate tissue characteristics. [73] In addition, the backscatter function may enhance feature detection using edge detection procedures. [74] Another approach to b-scan quality improvement is based on separating attenuation from the scatter using retinal b-scan images. [75] Earlier McDicken et al. used a conventional automatic gain control where amplifier gain was maintained by the integrated derived signal for ultrasound applications. [76, 77] Hughes and Duck developed an automatic compensation procedure assuming a linear relationship between attenuation and backscatter. [1] Further, Girard et al. successfully applied this procedure for OCT attenuation compensation. [8]

Recently an automated, depth resolved estimation of attenuation has been proposed where invertible mapping is used between the measured OCT intensity data and the attenuation coefficient by Depth-Resolved Confocal (DRC) function. For accurate measurements of attenuation coefficient in practical settings, confocal function and sensitivity fall-off were taken into account. [78]

Another important reason for attenuation is due to system noise which hampers image resolution and sometimes creates unnecessary details. Inverse filtering can be used to increase high frequency noise component. As a result, signal to noise ratio will be lower at higher frequencies. At higher frequencies, signal is weaker than noise. Considering noise, several decomposition algorithms have been proposed. [79-84]

4. METHODS

4.1. Subjects and Datasets:

4.1.1 Fundus Photography of the Optic Nerve Head

Two dimensional stereo-photography (TRC-SS; Topcon Instruments Corp. of America, Paramus, NJ) of the optic nerve head of fifty-five study eyes from the University of California San Diego (UCSD) Diagnostic Innovations in Glaucoma Study (DIGS) were used for our 2-D study of retinal vascular structure. The UCSD Institutional Review Board approved the study methodologies, and all methods adhered to the Declaration of Helsinki guidelines for research in human subjects and the Health Insurance Portability and Accountability Act (HIPAA).

4.1.2 OCT Data Collection:

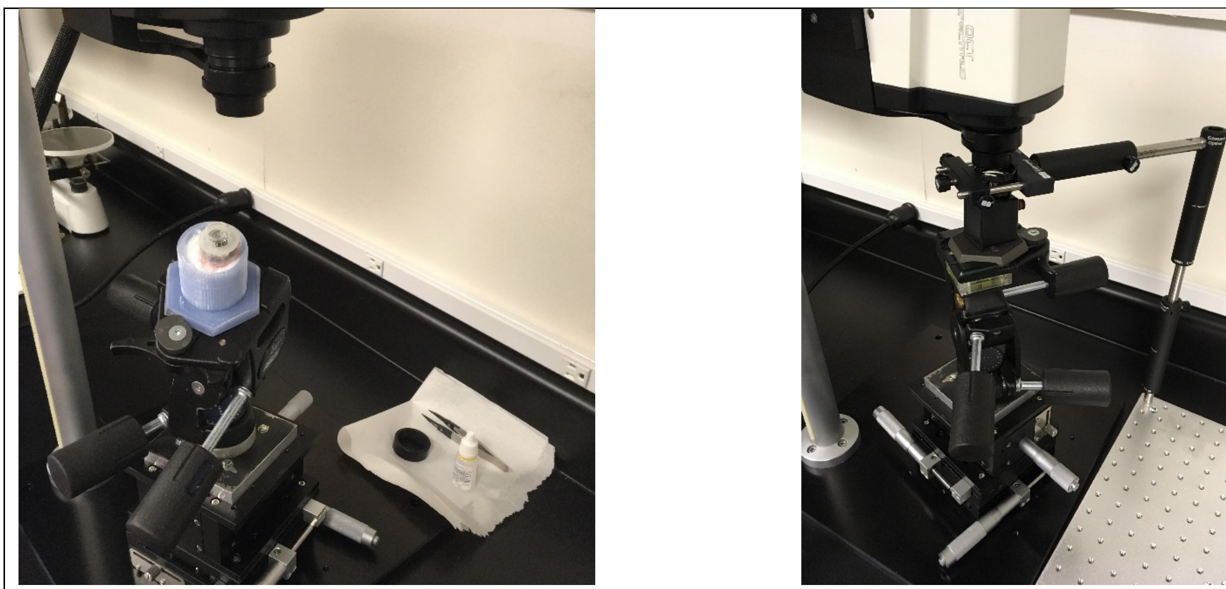

(a) (b)

Figure 4.1: Spectral Domain Optical Coherence Tomography (Spectralis, Heidelberg Engineering, GmbH) setup for imaging porcine eyes. (a) The retina of the study eyes was imaged either using an artificial cornea or keratoprosthesis or (b) isolated retinal tissues were images using an 60D external maxfield lens with the tissue immersed in saline.

Three-dimensional scans of five porcine eyes were used in this study [43, 85]. Porcine eyes were obtained (in PBS) from a USDA inspected meat processing facility within 4 hours after harvesting. In the experimental eyes, the central cornea was trephined (8.5 mm), lens removed and vitreous replaced (Intrector, Insight Instruments, Inc) rapidly with saline. The corneal opening was sealed with a custom made 67 D keratoprosthesis that replaced the effective refractive power of the eye. Eyes were mounted on a gimbal with 6 degrees of freedom of movement. Spectralis SD-OCT (Heidelberg Engineering, GmbH) arrangement was modified to allow continuous imaging of the optic nerve head in ex vivo porcine eyes. Volume scans were obtained with a uniform A and B-scan resolution of 11 microns.

4.2. ATTENUATION OF OCT LIGHT TRANSMISSION:

As OCT signal propagates through a tissue, a small portion of it is converted into heat through absorption while the rest scatters in multiple directions including scatter in the forward and backward direction. The absorption and scattering properties of the sample is dependent on the OCT light wavelength as well as the constitutive elements of the tissue. In the following section, a brief outline of an OCT signal propagation model based on the ultrasound propagation model [1], a currently available attenuation compensation procedure developed by Girard et al [2] and an improvement to the attenuation compensation are presented.

4.2.1 <u>OCT Light Propagation Model within a Tissue:</u>

Let, x represent any spatial location within the tissue; $S(x)$ represent OCT signal amplitude at x. Light propagation through a tissue is governed by optical properties of its constitutive elements. Let, $a(x)$ be an attenuation function representing the fractional loss of OCT signal amplitude due to per unit distance travel through the tissue from location x to $x + \delta x$. Assuming that δx is small, the signal amplitude at $S(x+\delta x)$ can be approximated as [1]:

$$S(x+\delta x) = S(x) - S(x)\, a(x)\, \delta x \qquad (4.1)$$

$$S(x+\delta x) - S(x) = -\, S(x)\, a(x)\, \delta x$$

$\delta S = -a(x)\, S(x)\, \delta x$; dividing both sides by δx

$\frac{\delta S}{\delta x} = -a(x)\, S(x)$; taking limit $\delta x \to 0$

$$\frac{ds(x)}{dx} = -a(x)S(x) \qquad (4.2)$$

From equation (4.2) we can get a first order differential equation governing the transport of OCT signal within a biological tissue with an optical attenuation function $a(x)$.

$$\frac{ds(x)}{dx} + a(x)\, S(x) = 0$$

$\frac{ds(x)}{dx}\mu(x) + \mu(x)a(x)S(x) = 0$, where, $\mu(x)$ is an integrating factor

Let, $\mu'(x) = \mu(x)\, a(x)$, where prime represents a derivative with respect to x. Then,

$$\frac{ds(x)}{dx}\mu(x) + \mu'(x)S(x) = 0$$

$\left(S(x)\, \mu(x)\right)' = 0$, using product rule for derivatives

$S(x)\, \mu(x) = C$, after integrating on both sides

$$S(x) = \frac{C}{\mu(x)} \qquad (4.3)$$

Because $\mu(x)\, a(x) = \mu'(x)$

$$\mu'(x)\, /\mu(x) = a(x)$$

$\left(ln\, \mu(x)\right)' = a(x)$, since $\left(ln\, \mu(x)\right)' = \frac{d}{dx}\left(ln\, \mu(x)\right) = \frac{1}{\mu(x)}\frac{d}{dx}\mu(x) = \frac{\mu'(x)}{\mu(x)}$

$ln\, \mu(x) = \int a(u)du + k$, integrating on both sides

$\mu(x) = e^{\int a(u)\, du\, +\, k}$, taking exponential on both side

$$\mu(x) = e^k e^{\int a(u)du}$$

$$\mu(x) = k\, e^{\int a(u)du}$$

Substituting $\mu(x)$ in equation (4.3),

$$S(x) = \frac{C}{ke^{\int a(u)du}}$$

At x_0,

$$S(x_0) = \frac{c}{k} e^{-\int_{x_0}^{x_0} a(u)du}$$

$$S(x_0) = \frac{c}{k}$$

$$\therefore\ S(x) = S(x_0) e^{-\int_{x_0}^{x} a(u)du} \tag{4.4}$$

Here, the OCT signal amplitude at any location x within a tissue $S(x)$ is represented with respect to the amplitude at a reference location x_0, $S(x_0)$. Therefore, it can be observed from equation (4.4) that a fraction of the reference signal $S(x_0)$ proportional to the negative exponential of the tissue attenuation function $a(x)$ will be lost while propagating from reference location x_0 to x.

4.2.2 Model for OCT Signal Backreflected from the Tissue

Part of the OCT signal $S(x)$ at each location x is backscattered in the direction of the receiver. The level and magnitude of backscatter from a location is dependent on the optical scattering properties of the tissue at that location. Let, $b(x)$ represent the backscatter function at location x indicating the proportion of OCT signal $S(x)$ backreflected at that location x, i.e. $b(x)S(x)$ is backreflected from location x to the receiver at location x_0. Following the light propagation estimation procedure described above, the transport of the backreflected light $b(x)S(x)$ from x back to x_0 can be modeled as a first order ODE whose solution provides the equation governing the backreflected or backscattered light from x reaching the receiver located at x_0 as follows:

$$R(x) = S(x_0)\ b(x)\ e^{-2\int_{x_0}^{x} a(u)\ du} \tag{4.5}$$

where, $S(x_0)$ is the amplitude of the original transmitted signal, $b(x)$ is the backscatter function of the tissue, and the factor 2 in the exponent represents signal attenuation during forward propagation and backscatter of the OCT signal.

4.2.3 <u>OCT Attenuation and Shadow Artificats:</u>

From equation 4.5, it is evident that tissue locations with stronger attenuation will significantly attenuate the OCT signal backreflected to the receiver. Figure 4.2 shows an example of the effects of stronger OCT signal attenuation due to a blood vessel in the OCT signal path. It is desirable to remove these shadow artifacts from the OCT scans to provide a uniform spatial resolution of the tissue being imaged for diagnosis and management of ocular conditions.

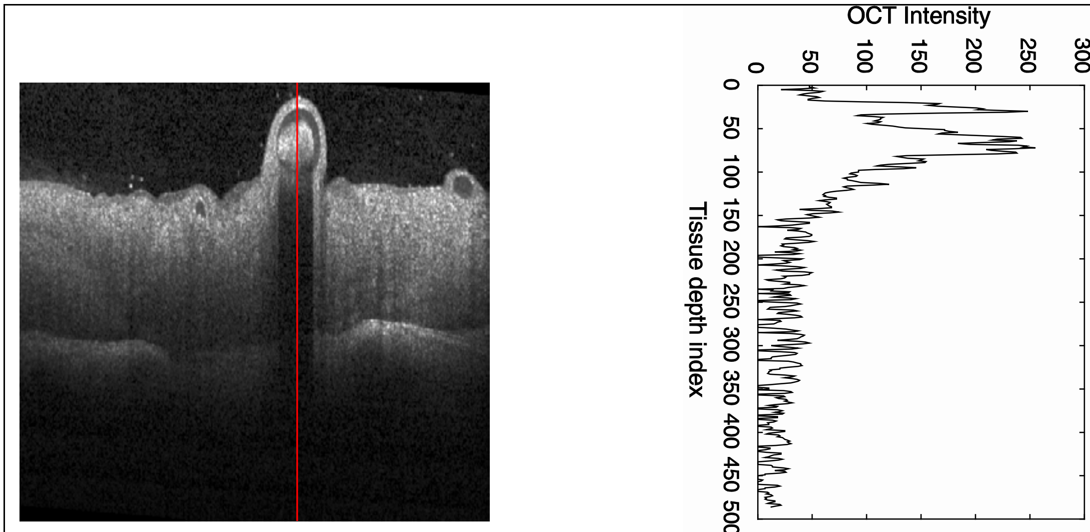

(a) (b)

Figure 4.2: A-scan (b) profile along a blood vessel location in the b-scan (a) illustrate the effects of OCT signal attenuation by the blood vessel causing a shadow artifact in the b-scan (a)

4.2.4 <u>OCT Attenuation Compensation Procedure by Girard [2]:</u>

To remove the shadow artifacts from ultrasound scans, Hughes and Duck [1] developed an attenuation compensation procedure. To resolve all the tissue structure uniformly, Hughes and Duck leveraged the fact that the signal received is governed by the spatial backscatter characteristics of the tissue given by $b(x)$. Therefore, a direct estimate of the tissue's backscatter function $b(x)$ will provide superior tissue information in contrast to the received signal $R(x)$ that is highly dependent on the signal attenuation. A brief description of the procedure for estimating the tissue backscatter $b(x)$ is provided below as in Hughes and Duck [1].

The received signal $R(x)$ is available from the ultrasound scanner as an a-scan and may be affected by the tissue attenuation characteristics $a(x)$ as given in equation 4.5. In general, $a(x)$ is unknown. Therefore, the attenuation $a(x)$ and backscatter $b(x)$ functions are assumed to be linearly related.

$a(x) = A + Bb(x)$, where A and B are unknown constants.

Substituting $a(x)$ in equation 4.5,

$$R(x) = S(x_0)\, b(x)\, e^{-2Ax-2B\int_{x_0}^{x} b(u)\, du}$$

$$R(x)\, e^{2Ax} = S(x_0)\, b(x)\, e^{-2B\int_{x_0}^{x} b(u)\, du} \qquad (4.6)$$

From equation 4.6, the backscatter function $b(x)$ can be recovered as,

$$b(x) = \frac{R(x) e^{2Ax}}{2B\int_{x}^{\infty} R(u)\, e^{2Au}\, du} \qquad (4.7)$$

where, B is an arbitrary constant and can be assumed to be unity. The denominator term forms the compensating signal

$$C(x) = 2B\int_{x}^{\infty} R(u)\, e^{2Au}\, du \qquad (4.8)$$

to compensate for attenuation.

Girard et al. [1] adapted the attenuation compensation procedure from Hughes and Duck to remove shadow artifacts. One of the limitations of the compensating signal given in equation 4.8 is integrating the received signal $R(x)$ from x to ∞. For example, in Fig. 4.2 b, this integral at a deeper location will correspond to a very small value due to system noise. Therefore, division by this low compensating factor may amplify the noise in those locations and hence the backscatter function $b(x)$ may be less useful.

4.2.5 *Backscatter Estimation from the Integral Equation:*

To overcome noise amplification in the deeper tissue locations, we reframed the governing equation of the received signal in equation 4.5 in the form of an integral equation with an exponential non-linearity as follows.

Taking logarithm on both sides of equation 4.5,

$$\log R(x) = \log\ [S_0\ e^{-2Ax}] + \log[b(x)] + \int_0^x (-2B) b(u) du$$

Rearranging the unknown backscatter terms $b(x)$ on the left hand side,

$$\log b(x) + \int_0^x (-2B) b(u) du = \log \frac{R(x)\ e^{2Ax}}{S_0} \tag{4.9}$$

Let,

$$k(x) = \log b(x) \ \Rightarrow b(x) = \ e^{k(x)}$$

$$f(x) = \log \frac{R(x)\ e^{2Ax}}{S_0}$$

$$g(x) = \ -2B$$

Substituting in equation 4.9,

$$k(x) + \int_0^x g(u)\ e^{k(u)}\ du = f(x)$$

This is an integral equation of the unknown function $k(x)$ with exponential non-linearity whose solution is readily available as follows (Sec. 5.4.1 in [86]).

$$k(x) = f(x) - \log\left[1 + \int_0^x g(u)\ e^{f(u)}\ du\right]$$

Substituting the expressions of $k(x), f(x) and\ g(x)$ and taking exponent on both sides,

$$\text{Backscatter } b(x) = \ R(x)\ e^{2Ax} / \left[S_0 - \ 2B\ \int_0^x R(u) e^{2Au}\ du\right] \tag{4.10}$$

In this study, we estimated the source signal amplitude for each a-scan $R(x)$ as $S_0 = \max[R(x)] + 10$. To further minimize noise amplification and/or suppress noise artifacts, we identified the bottom extent T of the signal $R(x)$ in each a-scan using a cumulative sum (CUSUM) based segmentation (or change point detection) approach [87] and evaluated the integral in equation 4.10 with an upper tissue depth limit of integration T.

4.3. Vessel Enhancement and Extraction Using Frangi Filter:

To extract vascular structure from 2D photographs of the retina and 3D OCT volume scans, we first enhanced the vessel structure and estimated a probabilistic measure of vesselness in each of the retinal locations using the *Frangi* filter [88]. A brief description of the operation of the Frangi filter is given below.

Vascular structures in 2D and 3D can be detected by inspecting local curvature measures in the images. Curvature information in images can be estimated using numerous directional filters as in the matched filter approach [42]. Instead of probing the image data with various directional filters, preferred orientation of curvature at a given location in the data can be directly identified by eigen analysis of the local Hessian matrix containing second derivatives in the x, y, z, xy, yz, and xz directions in 3D (a similar approach was also used for 2D). Using eigen analysis, specific direction and magnitude of local curvature can be directly estimated based on the estimates of curvatures in the standard x, y and z directions (given in the Hessian matrix for each data location).

Fig. 4.3b shows an illustration of the eigenvalue decomposition of the Hessian matrix at a given location. Eigenvectors corresponding to the largest eigenvalues correspond to directions across a vessel and the eigenvector with the least eigenvalue correspond to the direction along a vessel because, in most cases, the local vessel curvature are lower along the vessel compared to the curvature across a blood vessel.

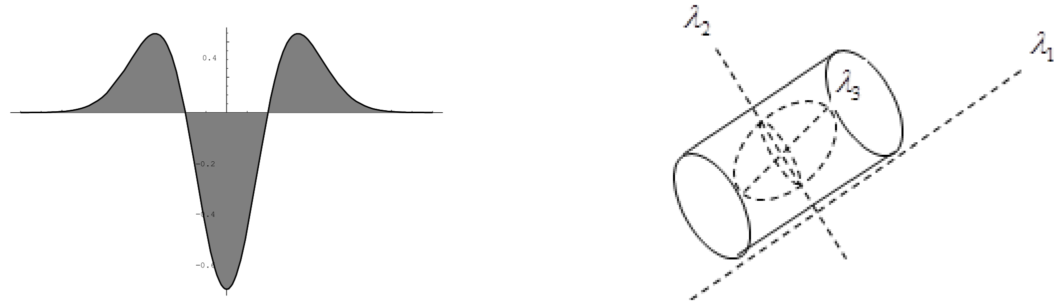

(a) (b)

Figure 4.3: (a) The second order derivative of a Gaussian kernel probes inside/outside contrast of the range ($-\sigma$, σ). In this example σ = 1. (b) The second order ellipsoid describes the local principal directions of curvature. Source: Frangi, et al. [88]

In case of two-dimensional vessel structures in retinal photographs, there are two eigenvalues $\{\lambda_1, \lambda_2\}$ and for three-dimensional vessel structures, there are three eigenvalues $\{\lambda_1, \lambda_2, \lambda_3\}$. Table 1 summarizes the characteristics of the eigenvalues in 2-D and 3-D with respect to the geometry of the local structure present in the images.

Table 1 Eigenvalues and likely orientation of local curvatures in 2-D and 3-D. N = noisy, L = Low, H = high and (+) and (-) indicates sign of eigen value. Source: Frangi, et al. [88]

2-D		**3-D**			**Orientation pattern**
λ_1	λ_2	λ_1	λ_2	λ_3	
N	N	N	N	N	Noisy, no preferred direction
		L	L	H-	Plate-like structure (bright)
		L	L	H+	Plate-like structure (dark)
L	H-	L	H-	H-	Tubular structure (bright)
L	H+	L	H+	H+	Tubular structure (dark)
H-	H-	H-	H-	H-	Blob-like structure (bright)
H+	H+	H+	H+	H+	Blob-like structure (dark)

Using the eigenvalues of the local curvature information, vesselness geometric ratios were estimated as

$$R_B = \frac{\lambda_1}{\lambda_2} \text{ in 2-D}$$

$$= \frac{|\lambda_1|}{\sqrt{|\lambda_2 \lambda_3|}} \text{ in 3-D}$$

$$R_A = \frac{|\lambda_2|}{|\lambda_3|} \text{ in 3-D}$$

Second geometric ratio indicates the grayscale level which will always remain constant under any type of intensity re-scaling. From here, we can state that our geometric ratio will only cover geometric information of the image. If vessel structure is not brighter than background then the response at a background pixel/voxel location is due to random noise. We eliminate the problem by working on the properties of background image. Magnitude of the derivatives of background image are less in our signal to noise ratios. To get rid of random noise response, we use the norm of the hessian.

Frobenius norm of the Hessian matrix when expressed in terms of the eigenvalues provides a clear indication of the degree of local curvature in an image. The vector norm S gives a measure to test for the presence of a vessel in each location in the image.

$$S = \| H \|_F = \sqrt{\sum_{j \le D} \lambda_j^2}$$

Using the geometric ratios and the vector norm of the local Hessian matrix, a probabilistic measure of vesselness measure is provided by the Frangi filter as follows.

Vesselness measure in 2-D:

$$V_0(s) = \begin{cases} 0 & \text{if } \lambda_2 > 0 \\ \exp(-\frac{{R_B}^2}{2\beta^2})(1-\exp(-\frac{S^2}{2c^2})) & \end{cases}$$

where β and c are thresholds which control sensitivity of line filter for measuring R_B and S.

Vesselness measure in 3-D:

$$V_0(s)=\begin{cases}0 & \text{if } \lambda_2>0 \text{ or } \lambda_3>0\\ ((1-\exp(-\frac{{R_A}^2}{2\alpha^2}))\exp(-\frac{{R_B}^2}{2\beta^2})(1-\exp(-\frac{s^2}{2c^2})) & \end{cases}$$

where α , β and c are thresholds which control sensitivity of line filter for measuring R_A , R_B and S .

4.3.1 <u>Scale-space Analysis of Vascular Structure:</u>

Frangi filter further employs scale-space theory to detect vessels of varying diameters by estimating spatial derivatives of images $I(w)$ using separable Gaussian filters of varying scales (or standard deviation) [89, 90]. Directional directives at various scales σ were computed by convolving the input image $I(w)$ with corresponding directional second derivative Gaussian filter.

$$\frac{d}{dw}I(w,\sigma)=\sigma^{\gamma}I(w)*\frac{d}{dw}G(w,\sigma)$$

Where,

$$G(w,\sigma)=\frac{1}{(2\pi\sigma^2)^{M/2}}e^{-\frac{|x|^2}{2\sigma^2}}$$

M indicating the dimension of the Gaussian kernel (2 or 3)

γ is used in multiple scales analysis.

5. RESULTS

The OCT attenuation compensation procedures were validated using: 1) numerically simulated a-scans, 2) SD-OCT b-scans of porcine eyes and 3) SD-OCT volume scans of porcine eyes. Vessel enhancement and extraction procedures were validated using 2-D photographs of human retina as well as 3-D SD-OCT scans of porcine eyes. A detailed description of these results are as follows. Attenuation compensation and vessel extraction algorithms were implemented in Matlab. VolView software and Python with VTK libraries were used for 3D volume visualization and surface rendering.

5.1. OCT Attenuation Compensation:

For validating the attenuation correction procedure, a tissue structure was simulated with an attenuation function $a(x)$ and a source signal amplitude of $S(x_0) = 5$ units. Using the OCT signal propagation model given in equations 4.4 through 4.7, OCT signal $S(x)$, received signal $R(x)$, compensating signal $C(x)$ and the estimated backscatter function $b(x)$ were estimated. Figure 5.1 shows the results of the attenuation compensation procedure for the simulated signal. It can be observed the tissue attenuation $a(x)$ was fully recovered by the backscatter function $b(x)$.

Figure 5.2 shows the validation of the attenuation compensation procedure for an SD-OCT a-scan (1D compensation). Compensation procedure by Girard et al. significantly amplified the noise at the signal boundary and hence require adaptive spatial thresholding as shown in Fig. 5.2c. The modified procedure provides an optimal enhancement of the SD-OCT a-scan signal throughout the spatial extent of the a-scan as shown in Fig. 5.2f. Attenuation compensation for an SD-OCT b-scan and a volume scan are shown in Figures 5.3 and 5.4, respectively. Similar to the 1-D compensation procedure, the modified attenuation compensation procedure provided an optimal and uniform compensation in both the axial and transverse spatial extents.

Figure 5.5 shows the results of the attenuation compensation procedure for the SD-OCT volume scans of the optic nerve head and retina.

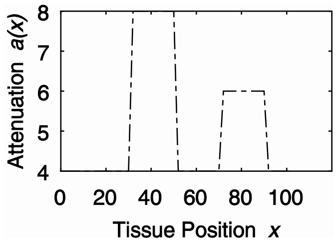

a) Assumed signal attenuation $a(x)$

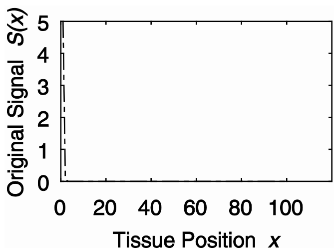

b) Signal $S(x)$ propagation tissue

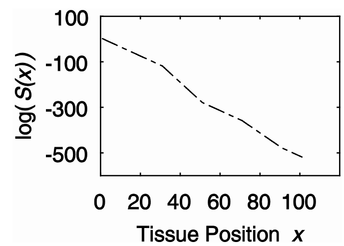

c) Log compressed signal $S(x)$

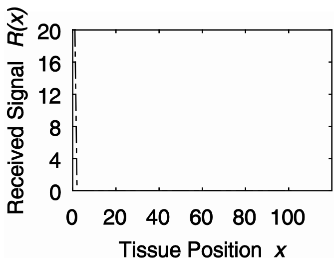

d) Backscattered signal $R(x)$ at receiver

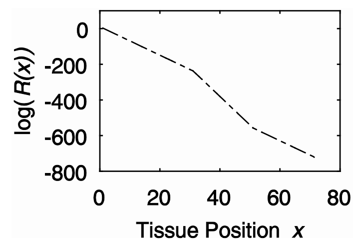

e) Log compressed signal $R(x)$

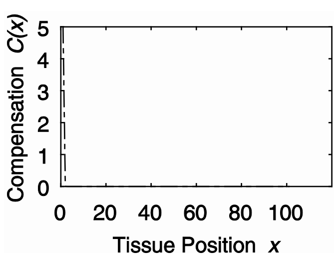

f) Compensating signal $C(x)$

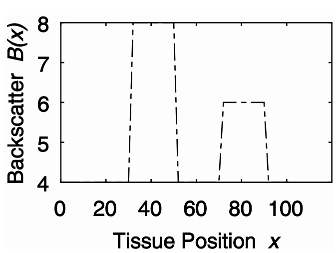

g) Estimate of backscatter $b(x)$

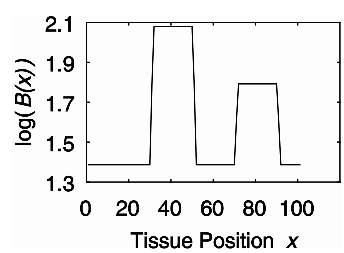

h) Log compressed backscatter

Figure 5.1: Validation of the OCT attenuation correction using a simulated signal $S(x)$ propagating through a tissue with a simulated signal attenuation coefficient $a(x)$. With $a(x) = b(x)$, we can recover the tissue backscatter $b(x)$ as $b(x) = R(x) / C(x)$

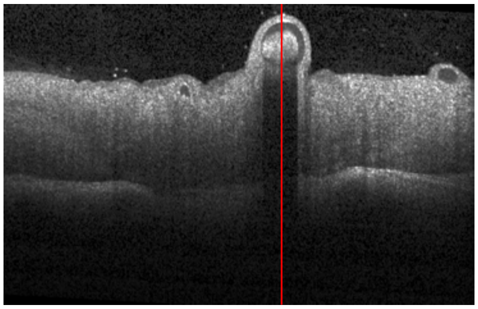

a) OCT b-scan. Red line indicates the location of the a-scan used for illustrating the attenuation compensation procedure.

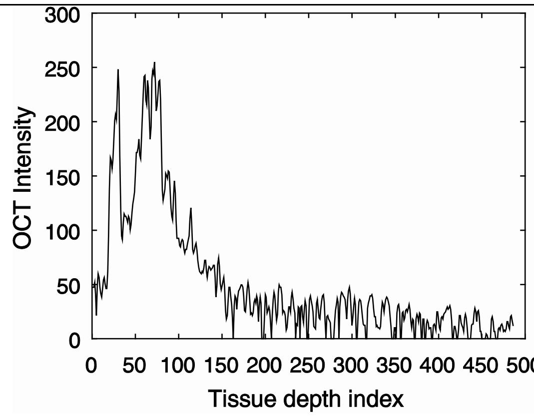

b) Observed a-scan $R(x)$ from the location shown in Fig. a)

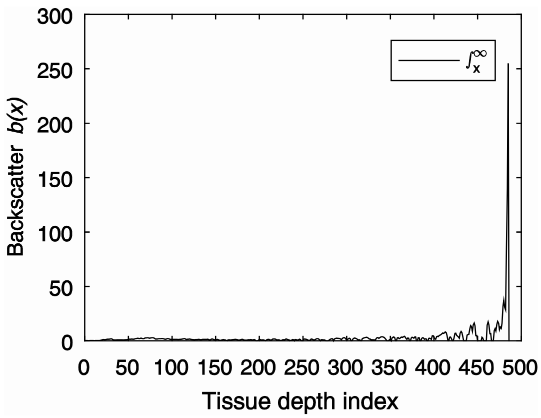

c) Compensating signal $C(x)$ obtained from x to ∞ integral

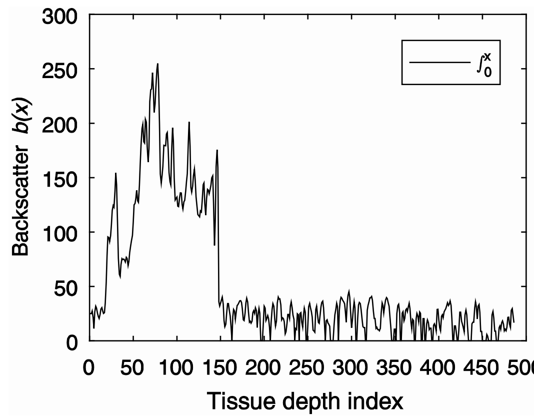

d) Compensating signal $C(x)$ from 0 to x integral with constant $A = 0.001$

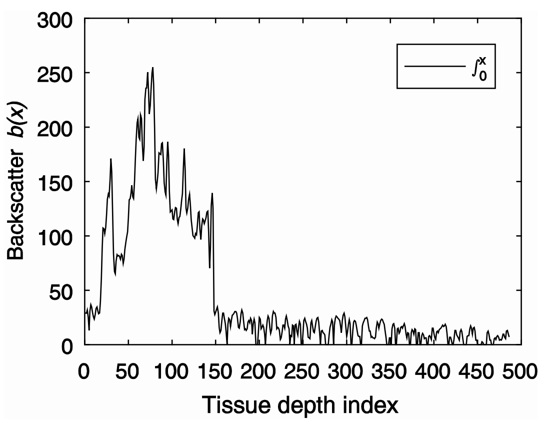

e) Compensating signal $C(x)$ from 0 to x integral with constant $A = 0$

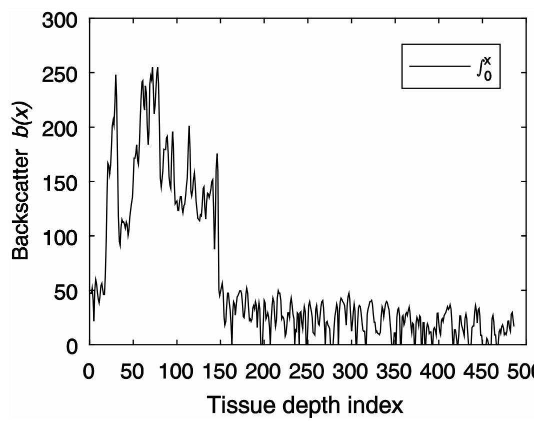

f) Backscatter $b(x)$ based on maximum signal among Figs. b), d), and e)

Figure 5.2: Validation of the OCT attenuation correction procedure using SD-OCT a-scans of a porcine eye. (f) Backscatter $b(x)$ significantly improves over (b) the received signal $R(x)$

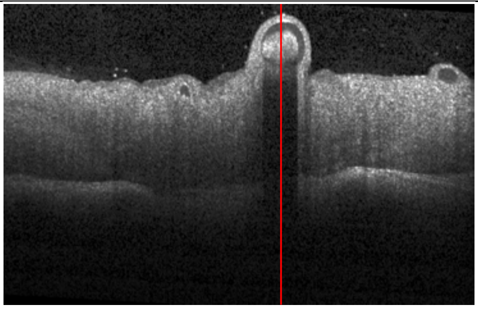

a) Observed SD-OCT b-scan

b) Backscatter with compensating integral from x to ∞

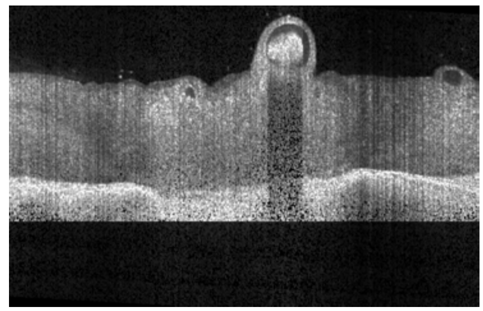

c) Backscatter with compensating integral from 0 to x and $A = 0.001$

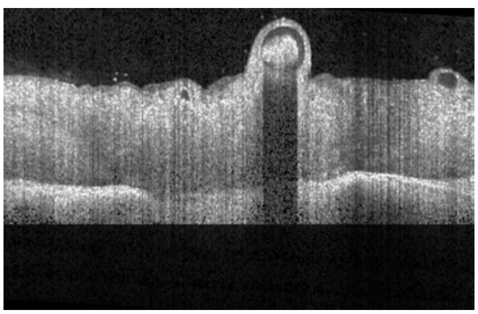

d) Backscatter with compensating integral from 0 to x with $A = 0$

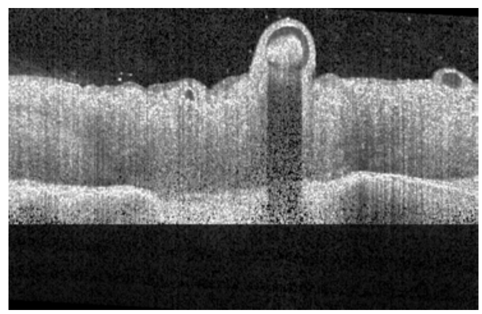

e) Backscatter as maximum local response among Figs. a), c), and d)

Figure 5.3: Validation of the attenuation correction procedure using SD-OCT b-scans of a porcine eye. (e) Backscatter $b(x)$ significantly improves over (a) the received signal $R(x)$ in both inner and outer retinal regions. (b) Poor compensation for attenuation was observed when the compensating signal calculation was based on integral through the full image depth ($x = \infty$).

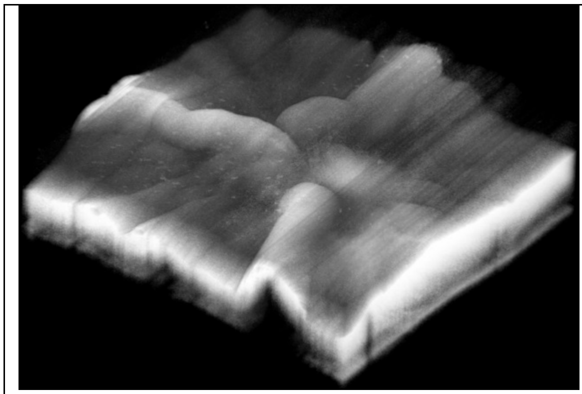

(a) Original SD-OCT scan

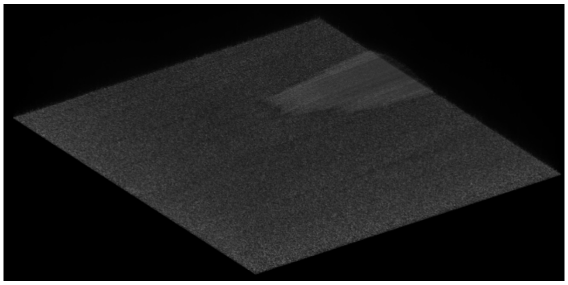

(b) Compensation using Girard et al

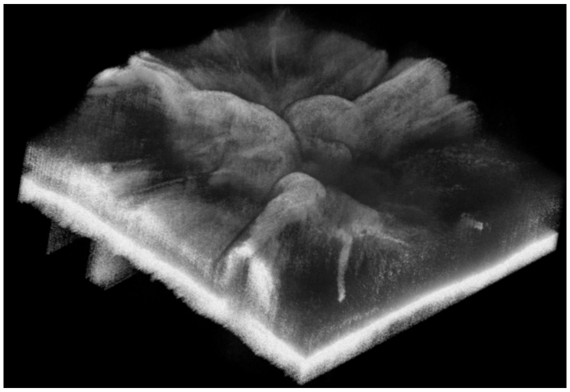

(c) Modified compensation with A = 0.001

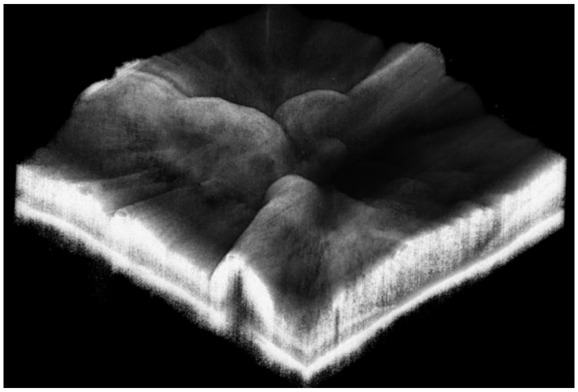

(d) Modified compensation with A = 0

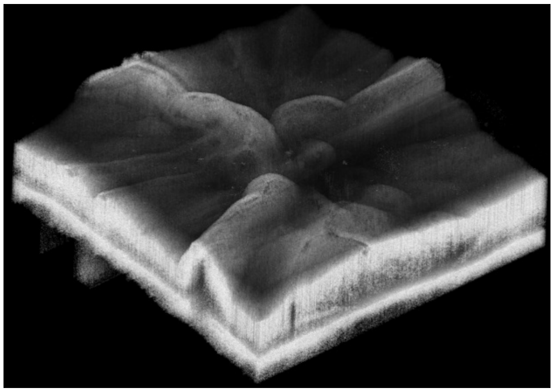

(e) Modified compensation combining (a), (c) and (d)

Figure 5.4: Attenuation correction for a 3D SD-OCT scan. (b) Girard et al procedure significantly amplified the noise near the signal boundary and hence the scan was not rendered. Using the modified procedure, it can be observed that constant A = 0.001 (c) enhances the deeper structures while losing signal strength in the anterior region; while A = 0 (d) enhances the whole depth equally. Combining the signal strength from the original signal (a), and modified procedures (c, d) provides an optimal attenuation correction at all depths (e).

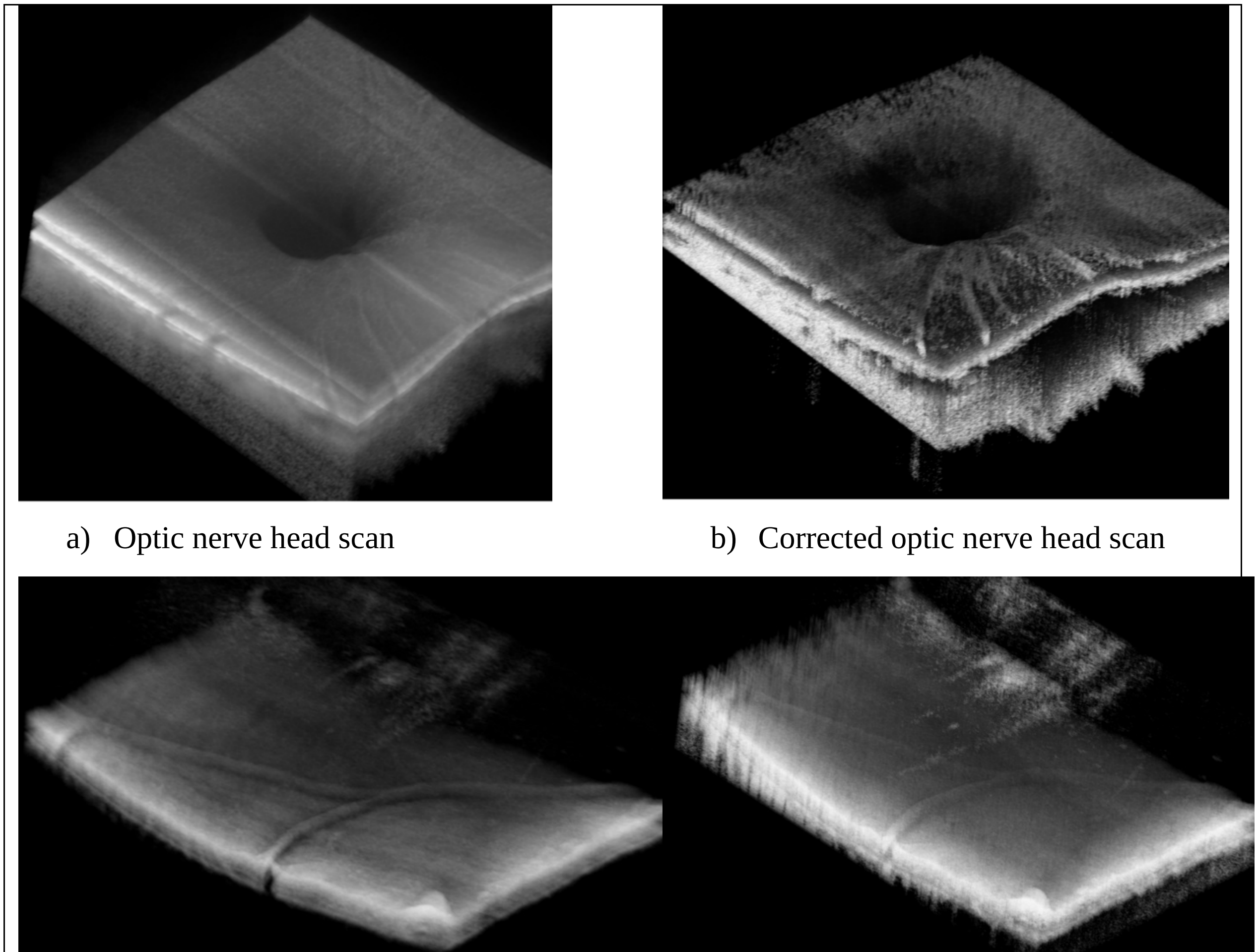

a) Optic nerve head scan b) Corrected optic nerve head scan

c) Retinal scan d) Corrected retinal scan

Figure 5.5: Examples of attenuation correction in 3D SD-OCT volumes of the optic nerve head (a) and retina (c) using the modified attenuation compensation procedure (b, d)

5.2. VESSEL EXTRACTION (2-D) FROM 2-D RETINAL PHOTOGRAPHS OF ONH:

Figures 5.6 and 5.7 show the 2-D vascular structure enhanced and extracted using the Frangi filter from 2D photographs of the optic nerve head of human subjects from the UCSD Diagnostic Innovations in Glaucoma Study. For scale-space analysis, pixel standard deviations ranging from 1 to 6 pixels were used. In some eyes, there were false positive vessel identification at the optic disk boundaries.

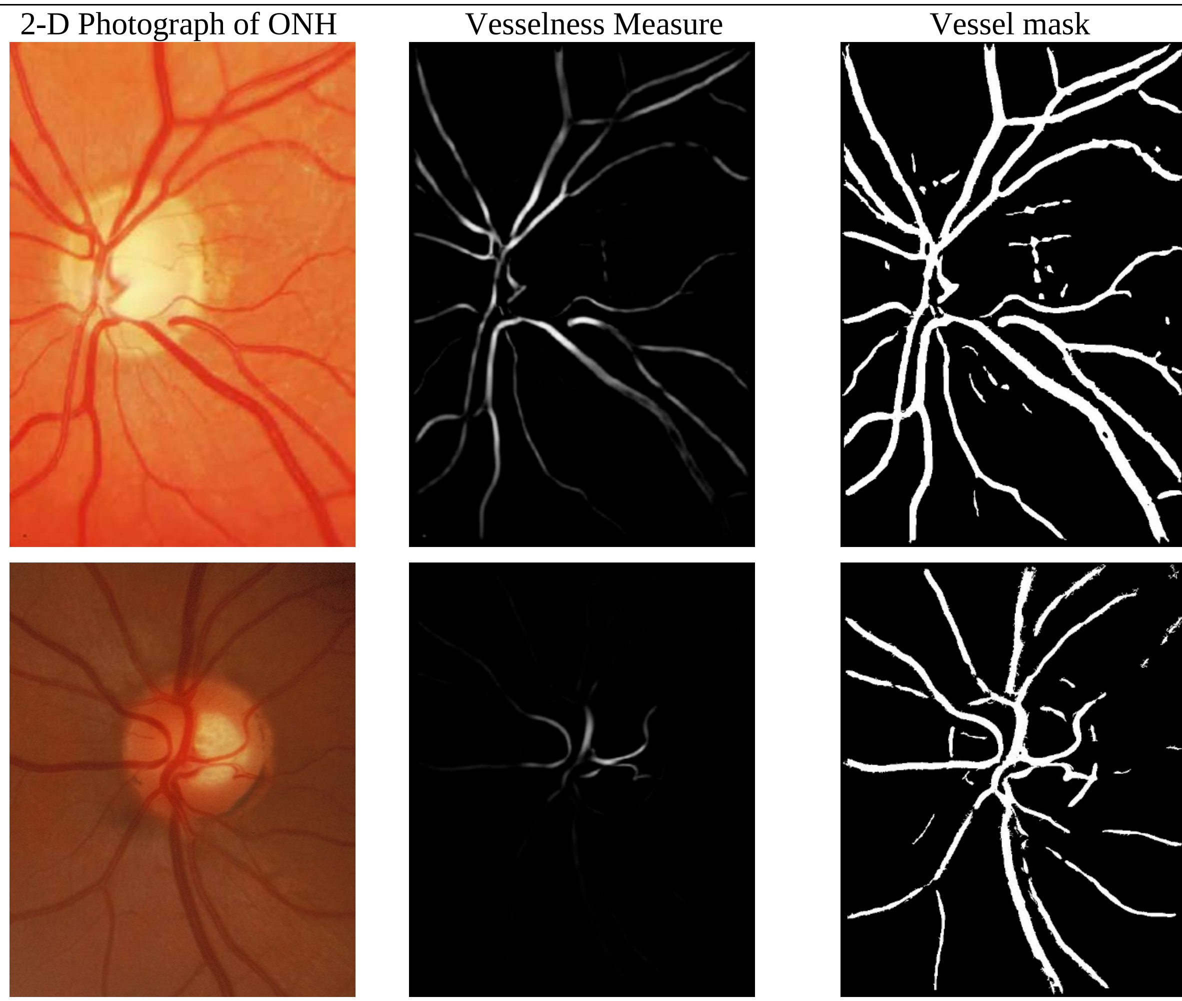

Figure 5.6: Retinal vasculature of the optic nerve head of human subjects enhanced and extracted using the Frangi filter

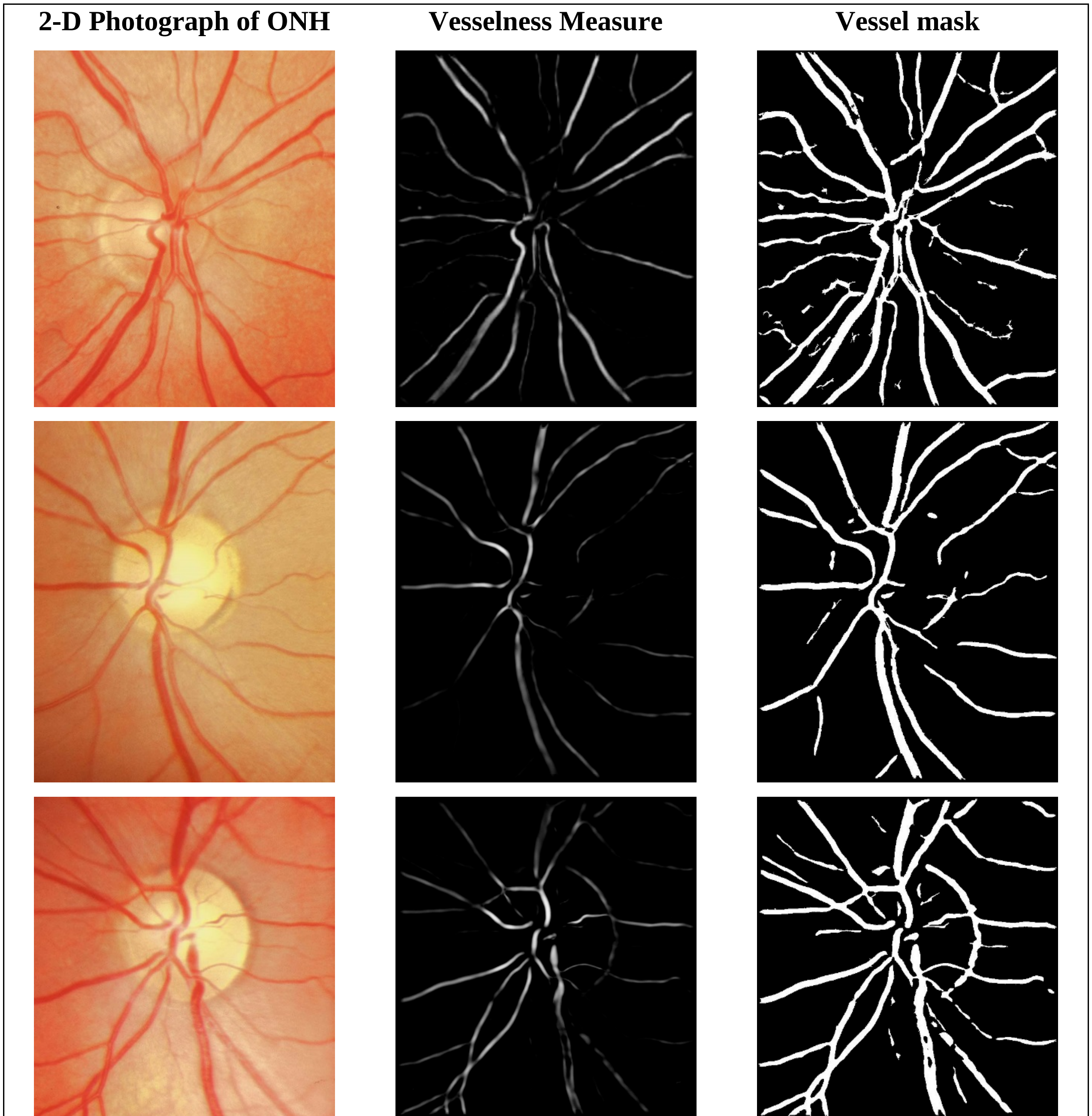

Figure 5.7: Retinal vasculature of the optic nerve head of human subjects enhanced and extracted using the Frangi filter

5.3. VESSEL EXTRACTION (3-D) FROM OCT DATA:

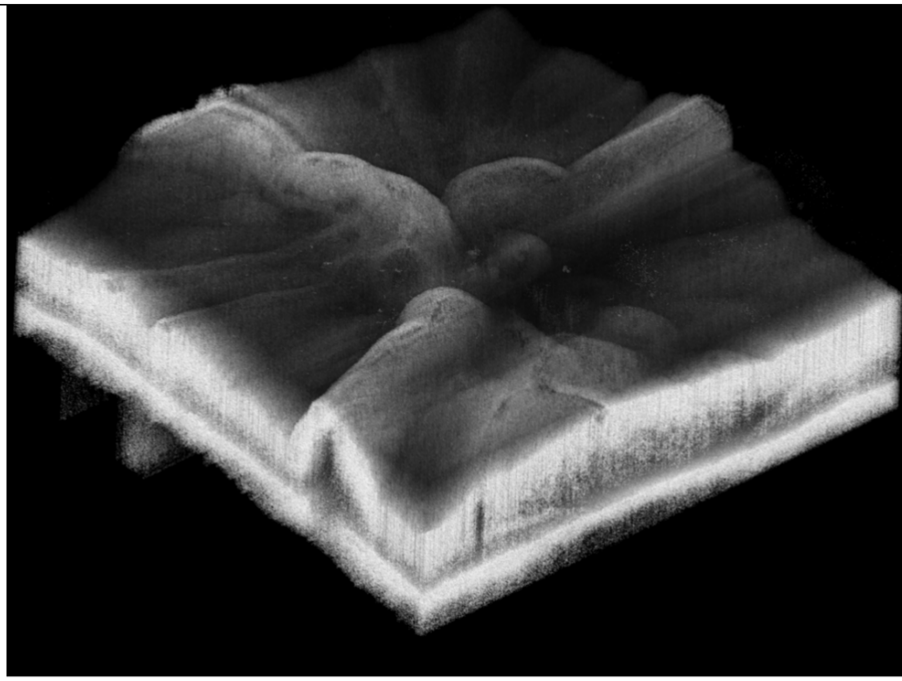

a) SD-OCT scan after attenuation compensation using the modified procedure

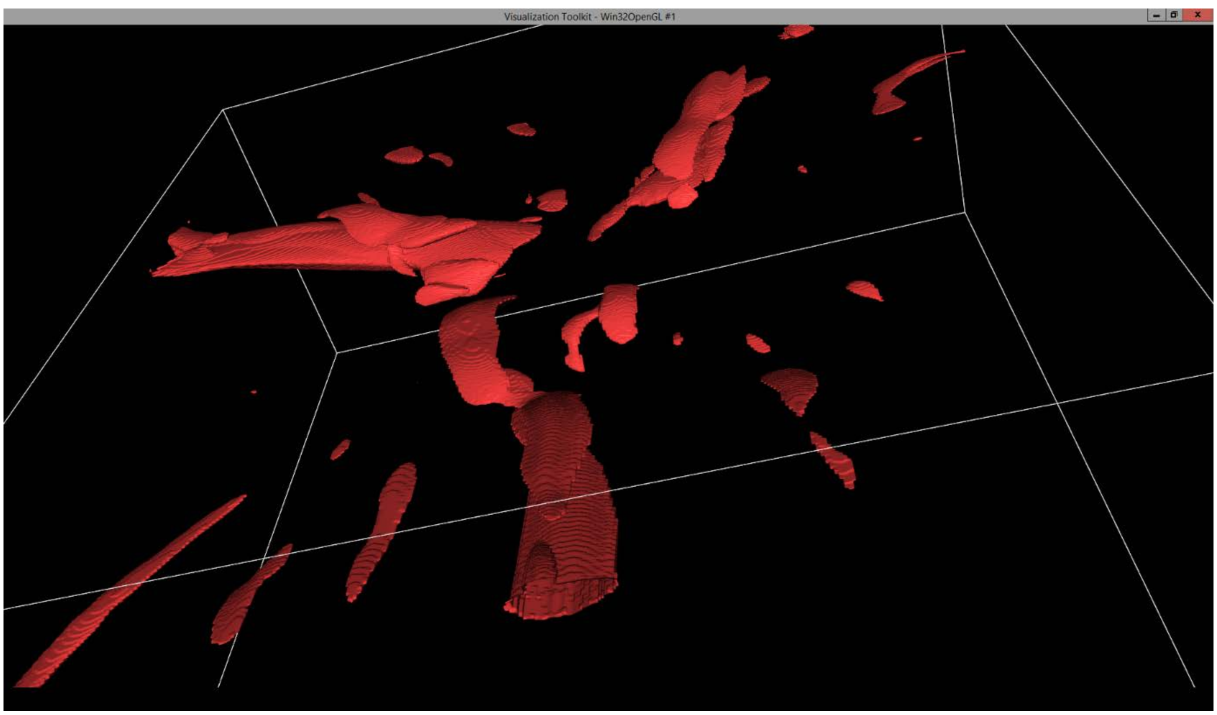

b) 3-D vessel extraction from OCT data

c)

Figure 5.8: Major retinal vascular structure extracted using the Frangi filter (b) from the SD-OCT optic nerve head scan (a) of a porcine eye

Figure 5.8 shows an SD-OCT scan of a porcine eye and the geometry of the major retinal vessels extracted after enhancing the vascular structure using Frangi filter. For this example eye, a scale of 40 was used to identify the vascular structure. Further, a vesselness threshold of 0.2 was used to extract the 3D vessel mask (Fig. 5.8 b) of the retinal vascular structure.

6. CONCLUSION

In this study, we have presented a modified attenuation correction procedure to compensate for OCT signal attenuation in tissues due to high optical absorption and/or scattering in the locations with retinal blood vessels and collagenous structures such as the lamina cribrosa of the retina. The attenuation correction procedure developed by Girard et al. highly amplifies the noise near the signal boundary and therefore requires adaptive spatial thresholding of the compensated data. By directly solving the integral equation with exponential non-linearity that govern the OCT light transport in tissue, the modified procedure presented in this study significantly minimizes noise amplification near the signal boundaries. Because of the adaptive nature of the attenuation compensation, the modified procedure is suitable for SD-OCT scans of the retina, optic nerve head as well as scans of the anterior segment of the eye.

Based on our observations, Frangi filter is suitable for extracting retinal vascular structure from both 2-D photographs and 3-D SD-OCT volume scans. Due to poor vessel contrast in the SD-OCT scans, it still remains a challenge to fully extract the vascular network using the Frangi filter. Future work may combine the results of the Frangi filter with a shape tracking algorithm to extract a more robust and complete vascular network of the retina. Both the attenuation compensation and blood vessel extraction techniques presented in this work are likely to be useful for automated analysis of optical images of the retina for aiding diagnosis and management of Glaucoma, diabetic retinopathy, and other neovascular diseases of the eye.

7. REFERENCES

[1] D. I. Hughes and F. A. Duck, "Automatic attenuation compensation for ultrasonic imaging," *Ultrasound in Medicine and Biology,* vol. 23, pp. 651-664, 1997.

[2] M. J. A. Girard, N. G. Strouthidis, C. R. Ethier, and J. M. Mari, "Shadow Removal and Contrast Enhancement in Optical Coherence Tomography Images of the Human Optic Nerve Head," *Investigative Ophthalmology & Visual Science,* vol. 52, pp. 7738-7748, Sep 2011.

[3] H. Kolb, E. Fernandez, and R. Nelson, "Bipolar Cell Pathways in the Vertebrate Retina--Webvision: The Organization of the Retina and Visual System," 1995.

[4] H. Kolb, "How the retina works," *American scientist,* vol. 91, pp. 28-35, 2003.

[5] J. Bergman and J. Calkins, *Is the Backwards Human Retina Evidence of Poor Design?*: Institute for Creation Research, 2005.

[6] D. N. Gangwar, I. S. Jain, and S. P. Dhir, "Course of the nerve fibres in the temporal half of the retina," *Indian J Ophthalmol,* vol. 25, pp. 17-9, Oct 1977.

[7] M. Balasubramanian, C. Bowd, and L. M. Zangwill, "Algorithms for Detecting Glaucomatous Structural Changes in the Optic Nerve Head," *Image Modeling of the Human Eye*, pp. 147-188, 2008.

[8] C. V. Network, "Developmental Anatomy of the Retinal and Choroidal Vasculature," *The retina and its disorders,* vol. 179, 2011.

[9] A. F. Fercher, C. K. Hitzenberger, W. Drexler, G. Kamp, and H. Sattmann, "In vivo optical coherence tomography," *American journal of ophthalmology,* vol. 116, p. 113, 1993.

[10] J. M. Schmitt, A. Knuttel, M. Yadlowsky, and M. A. Eckhaus, "Optical-Coherence Tomography of a Dense Tissue - Statistics of Attenuation and Backscattering," *Physics in Medicine and Biology,* vol. 39, pp. 1705-1720, Oct 1994.

[11] J. G. Fujimoto, M. E. Brezinski, G. J. Tearney, S. A. Boppart, B. Bouma, M. R. Hee, *et al.*, "Optical Biopsy and Imaging Using Optical Coherence Tomography," *Nature Medicine,* vol. 1, pp. 970-972, Sep 1995.

[12] J. M. Schmitt, M. J. Yadlowsky, and R. F. Bonner, "Subsurface Imaging of Living Skin with Optical Coherence Microscopy," *Dermatology,* vol. 191, pp. 93-98, 1995.

[13] K. Takada, I. Yokohama, K. Chida, and J. Noda, "New measurement system for fault location in optical waveguide devices based on an interferometric technique," *Applied optics,* vol. 26, pp. 1603-1606, 1987.

[14] R. C. Youngquist, S. Carr, and D. E. N. Davies, "Optical Coherence-Domain Reflectometry - a New Optical Evaluation Technique," *Optics Letters,* vol. 12, pp. 158-160, Mar 1987.

[15] A. F. Fercher, K. Mengedoht, and W. Werner, "Eye-Length Measurement by Interferometry with Partially Coherent-Light," *Optics Letters,* vol. 13, pp. 186-188, Mar 1988.

[16] C. K. Hitzenberger, W. Drexler, and A. F. Fercher, "Measurement of Corneal Thickness by Laser Doppler Interferometry," *Investigative Ophthalmology & Visual Science,* vol. 33, pp. 98-103, Jan 1992.

[17] J. A. Izatt, M. R. Hee, E. A. Swanson, C. P. Lin, D. Huang, J. S. Schuman, *et al.*, "Micrometer-Scale Resolution Imaging of the Anterior Eye in-Vivo with Optical Coherence Tomography," *Archives of Ophthalmology,* vol. 112, pp. 1584-1589, Dec 1994.

[18] X. Clivaz, F. Marquisweible, R. P. Salathe, R. P. Novak, and H. H. Gilgen, "High-Resolution Reflectometry in Biological Tissues," *Optics Letters,* vol. 17, pp. 4-6, Jan 1 1992.

[19] J. M. Schmitt, A. Knuttel, and R. F. Bonner, "Measurement of Optical-Properties of Biological Tissues by Low-Coherence Reflectometry," *Applied Optics,* vol. 32, pp. 6032-6042, Oct 20 1993.

[20] M. R. Hee, J. A. Izatt, E. A. Swanson, D. Huang, J. S. Schuman, C. P. Lin, *et al.*, "Optical Coherence Tomography of the Human Retina," *Archives of Ophthalmology,* vol. 113, pp. 325-332, Mar 1995.

[21] S. A. Boppart, M. E. Brezinski, B. E. Bouma, G. J. Tearney, and J. G. Fujimoto, "Investigation of developing embryonic morphology using optical coherence tomography," *Developmental Biology,* vol. 177, pp. 54-63, Jul 10 1996.

[22] J. A. Izatt, M. D. Kulkarni, H. W. Wang, K. Kobayashi, and M. V. Sivak, "Optical coherence tomography and microscopy in gastrointestinal tissues," *Ieee Journal of Selected Topics in Quantum Electronics,* vol. 2, pp. 1017-1028, Dec 1996.

[23] Y. Pan, E. Lankenau, J. Welzel, R. Birngruber, and R. Engelhardt, "Optical coherence gated imaging of biological tissues," *Ieee Journal of Selected Topics in Quantum Electronics,* vol. 2, pp. 1029-1034, Dec 1996.

[24] J. Welzel, E. Lankenau, R. Birngruber, and R. Engelhardt, "Optical coherence tomography of the human skin," *Journal of the American Academy of Dermatology,* vol. 37, pp. 958-963, Dec 1997.

[25] M. S. Natheem, R. Narayanan, and P. N. Nagaiyan, "Advanced face recognition system using Fourier Optics and Neural Networks," in *Wireless and Optical Communications Networks (WOCN), 2013 Tenth International Conference on*, 2013, pp. 1-3.

[26] A. G. Podoleanu, "Unbalanced versus balanced operation in an optical coherence tomography system," *Applied Optics,* vol. 39, pp. 173-182, Jan 1 2000.

[27] J. A. Izatt, M. A. Choma, and A.-H. Dhalla, "Theory of optical coherence tomography," *Optical Coherence Tomography: Technology and Applications,* pp. 65-94, 2015.

[28] K. Akita and H. Kuga, "A Computer Method of Understanding Ocular Fundus Images," *Pattern Recognition,* vol. 15, pp. 431-443, 1982.

[29] C. Sinthanayothin, J. F. Boyce, H. L. Cook, and T. H. Williamson, "Automated localisation of the optic disc, fovea, and retinal blood vessels from digital colour fundus images," *British Journal of Ophthalmology,* vol. 83, pp. 902-910, Aug 1999.

[30] S. Chaudhuri, S. Chatterjee, N. Katz, M. Nelson, and M. Goldbaum, "Detection of Blood-Vessels in Retinal Images Using Two-Dimensional Matched-Filters," *Ieee Transactions on Medical Imaging,* vol. 8, pp. 263-269, Sep 1989.

[31] I. E. Abdou and W. K. Pratt, "Quantitative Design and Evaluation of Enhancement-Thresholding Edge Detectors," *Proceedings of the Ieee,* vol. 67, pp. 753-763, 1979.

[32] J. Lee, R. Haralick, and L. Shapiro, "Morphologic edge detection," *IEEE Journal on Robotics and Automation,* vol. 3, pp. 142-156, 1987.

[33] D. Marr and E. Hildreth, "Theory of Edge-Detection," *Proceedings of the Royal Society Series B-Biological Sciences,* vol. 207, pp. 187-217, 1980.

[34] J. Canny, "A Computational Approach to Edge-Detection," *Ieee Transactions on Pattern Analysis and Machine Intelligence,* vol. 8, pp. 679-698, Nov 1986.

[35] V. Torre and T. A. Poggio, "On Edge-Detection," *Ieee Transactions on Pattern Analysis and Machine Intelligence,* vol. 8, pp. 147-163, Mar 1986.

[36] Y. A. Tolias and S. M. Panas, "A fuzzy vessel tracking algorithm for retinal images based on fuzzy clustering," *Ieee Transactions on Medical Imaging,* vol. 17, pp. 263-273, Apr 1998.

[37] C. Boldak, Y. Rolland, C. Toumoulin, and J. Coatrieux, "An improved model-based vessel tracking algorithm with application to computed tomography angiography," *Biocybernetics And Biomedical Engineering,* vol. 23, pp. 41-64, 2003.

[38] Y. Jiang, A. Bainbridge-Smith, and A. Morris, "Blood vessel tracking in retinal images," *Proceedings of image and Vision Computing,* vol. 126131, 2007.

[39] D. Marin, A. Aquino, M. E. Gegundez-Arias, and J. M. Bravo, "A New Supervised Method for Blood Vessel Segmentation in Retinal Images by Using Gray-Level and Moment Invariants-Based Features," *Ieee Transactions on Medical Imaging,* vol. 30, pp. 146-158, Jan 2011.

[40] F. P. Miles and A. L. Nuttall, "Matched-Filter Estimation of Serial Blood-Vessel Diameters from Video Images," *Ieee Transactions on Medical Imaging*, vol. 12, pp. 147-152, Jun 1993.

[41] L. A. Zhou, M. S. Rzeszotarski, L. J. Singerman, and J. M. Chokreff, "The Detection and Quantification of Retinopathy Using Digital Angiograms," *Ieee Transactions on Medical Imaging*, vol. 13, pp. 619-626, Dec 1994.

[42] A. Hoover, V. Kouznetsova, and M. Goldbaum, "Locating blood vessels in retinal images by piecewise threshold probing of a matched filter response," *Ieee Transactions on Medical Imaging*, vol. 19, pp. 203-210, Mar 2000.

[43] T. Chanwimaluang and G. Fan, "An efficient blood vessel detection algorithm for retinal images using local entropy thresholding," in *Circuits and Systems, 2003. ISCAS'03. Proceedings of the 2003 International Symposium on*, 2003, pp. V-V.

[44] M. Al-Rawi, M. Qutaishat, and M. Arrar, "An improved matched filter for blood vessel detection of digital retinal images," *Computers in Biology and Medicine*, vol. 37, pp. 262-267, Feb 2007.

[45] B. Zhang, L. Zhang, L. Zhang, and F. Karray, "Retinal vessel extraction by matched filter with first-order derivative of Gaussian," *Computers in Biology and Medicine*, vol. 40, pp. 438-445, Apr 2010.

[46] A. M. Mendonca and A. Campilho, "Segmentation of retinal blood vessels by combining the detection of centerlines and morphological reconstruction," *Ieee Transactions on Medical Imaging*, vol. 25, pp. 1200-1213, Sep 2006.

[47] M. Fraz, P. Remagnino, A. Hoppe, B. Uyyanonvara, C. Owen, A. Rudnicka, *et al.*, "Retinal vessel extraction using first-order derivative of Gaussian and morphological processing," *Advances in visual computing*, pp. 410-420, 2011.

[48] N. Kanopoulos, N. Vasanthavada, and R. L. Baker, "Design of an Image Edge-Detection Filter Using the Sobel Operator," *Ieee Journal of Solid-State Circuits*, vol. 23, pp. 358-367, Apr 1988.

[49] S. Ying, "Automated Identification of Vessel Contours in Coronary Arteriograms by an Adaptive Tracking Algorithm," *Ieee Transactions on Medical Imaging*, vol. 8, pp. 78-88, Mar 1989.

[50] A. Can, H. Shen, J. N. Turner, H. L. Tanenbaum, and B. Roysam, "Rapid automated tracing and feature extraction from retinal fundus images using direct exploratory algorithms," *IEEE Transactions on information Technology in Biomedicine*, vol. 3, pp. 125-138, 1999.

[51] P. M. J. van der Zwet, M. Nettesheim, J. J. Gerbrands, and J. H. C. Reiber, "Derivation of optimal filters for the detection of coronary arteries," *Ieee Transactions on Medical Imaging*, vol. 17, pp. 108-120, Feb 1998.

[52] W. Ohley, Y. Sun, A. Most, and D. Williams, "A computationally efficient algorithm for tracking coronary arteries on digital arteriograms," in *Proc. IEEE 11th Northeast Bioengineering Conf*, 1985, pp. 255-258.

[53] L. Gang, O. Chutatape, and S. M. Krishnan, "Detection and measurement of retinal vessels, in fundus images using amplitude modified second-order Gaussian filter," *Ieee Transactions on Biomedical Engineering,* vol. 49, pp. 168-172, Feb 2002.

[54] O. Chutatape, L. Zheng, and S. M. Krishnan, "Retinal blood vessel detection and tracking by matched Gaussian and Kalman filters," in *Engineering in Medicine and Biology Society, 1998. Proceedings of the 20th Annual International Conference of the IEEE*, 1998, pp. 3144-3149.

[55] T. Yedidya and R. Hartley, "Tracking of blood vessels in retinal images using Kalman filter," in *Computing: Techniques and Applications, 2008. DICTA'08. Digital Image*, 2008, pp. 52-58.

[56] H. G. Chen and J. Hale, "An Algorithm for Mr-Angiography Image-Enhancement," *Magnetic Resonance in Medicine*, vol. 33, pp. 534-540, Apr 1995.

[57] Y. P. Du, D. L. Parker, and W. L. Davis, "Vessel enhancement filtering in three-dimensional MR angiography," *Journal of Magnetic Resonance Imaging,* vol. 5, pp. 353-359, 1995.

[58] Y. P. Du and D. L. Parker, "Vessel enhancement filtering in three-dimensional MR angiograms using long-range signal correlation," *Journal of Magnetic Resonance Imaging,* vol. 7, pp. 447-450, 1997.

[59] S. Aylward, E. Bullitt, S. Pizer, and D. Eberly, "Intensity ridge and widths for tubular object segmentation and description," in *Mathematical Methods in Biomedical Image Analysis, 1996., Proceedings of the Workshop on*, 1996, pp. 131-138.

[60] G. Gerig, "Segmentation, Description and Analysis of the Cerebral Vascularity," SWISS FEDERAL INSTITUTE OF TECHNOLOGY ZÜRICH, 1995.

[61] T. M. Koller, G. Gerig, G. Szekely, and D. Dettwiler, "Multiscale detection of curvilinear structures in 2-D and 3-D image data," in *Computer Vision, 1995. Proceedings., Fifth International Conference on*, 1995, pp. 864-869.

[62] C. Lorenz, I. C. Carlsen, T. M. Buzug, C. Fassnacht, and J. Weese, "Multi-scale line segmentation with automatic estimation of width, contrast and tangential direction in 2D and 3D medical images," *Cvrmed-Mrcas'97,* vol. 1205, pp. 233-242, 1997.

[63] Y. Sato, S. Nakajima, H. Atsumi, T. Koller, G. Gerig, S. Yoshida, *et al.*, "3D multi-scale line filter for segmentation and visualization of curvilinear structures in medical images," *Cvrmed-Mrcas'97,* vol. 1205, pp. 213-222, 1997.

[64] C. K. Hitzenberger, "Optical Measurement of the Axial Eye Length by Laser Doppler Interferometry," *Investigative Ophthalmology & Visual Science,* vol. 32, pp. 616-624, Mar 1991.

[65] G. J. Tearney, M. E. Brezinski, B. E. Bouma, S. A. Boppart, C. Pitris, J. F. Southern, *et al.*, "In vivo endoscopic optical biopsy with optical coherence tomography," *Science,* vol. 276, pp. 2037-2039, Jun 27 1997.

[66] J. M. Schmitt, "Optical coherence tomography (OCT): A review," *Ieee Journal of Selected Topics in Quantum Electronics,* vol. 5, pp. 1205-1215, Jul-Aug 1999.

[67] A. G. Podoleanu, "Optical coherence tomography," *The British journal of radiology,* 2014.

[68] C. Y. Xu, J. M. Schmitt, S. G. Carlier, and R. Virmani, "Characterization of atherosclerosis plaques by measuring both backscattering and attenuation coefficients in optical coherence tomography," *Journal of Biomedical Optics,* vol. 13, May-Jun 2008.

[69] M. Hohmann, B. Lengenfelder, R. Kanawade, F. Klampfl, and M. Schmidt, "Extension of depth-resolved reconstruction of attenuation coefficients in optical coherence tomography for slim samples," *Biophotonics Japan 2015,* vol. 9792, 2015.

[70] S. A. Hojjatoleslami, M. R. N. Avanaki, and A. G. Podoleanu, "Image quality improvement in optical coherence tomography using Lucy-Richardson deconvolution algorithm," *Applied Optics,* vol. 52, pp. 5663-5670, Aug 10 2013.

[71] N. Dwork, G. T. Smith, J. M. Pauly, and A. K. E. Bowden, "Automated Estimation of OCT Confocal Function Parameters from two B-Scans," *2016 Conference on Lasers and Electro-Optics (Cleo),* 2016.

[72] D. J. Faber, F. J. van der Meer, M. C. G. Aalders, and T. G. van Leeuwen, "Quantitative measurement of attenuation coefficients of weakly scattering media using optical coherence tomography," *Optics Express,* vol. 12, pp. 4353-4365, Sep 20 2004.

[73] M. Odonnell, "Effects of Diffraction on Measurements of the Frequency-Dependent Ultrasonic-Attenuation," *Ieee Transactions on Biomedical Engineering,* vol. 30, pp. 320-326, 1983.

[74] H. E. Melton, S. M. Collins, and D. J. Skorton, "Automatic Real-Time Endocardial Edge-Detection in Two-Dimensional Echocardiography," *Ultrasonic Imaging,* vol. 5, pp. 300-307, 1983.

[75] F. Duck and C. Hill, "Mapping true ultrasonic backscatter and attenuation distribution in tissue—a digital reconstruction approach," in *Ultrasonic Tissue Characterization II,* ed, 1979, p. 247.

[76] W. N. Mcdicken, D. H. Evans, and D. A. Robertson, "Automatic Sensitivity Control in Diagnostic Ultrasonics," *Ultrasonics,* vol. 12, pp. 173-176, 1974.

[77] S. D. Pye, S. R. Wild, and W. N. Mcdicken, "Adaptive Time Gain Compensation for Ultrasonic-Imaging," *Ultrasound in Medicine and Biology,* vol. 18, pp. 205-212, 1992.

[78] G. T. Smith, N. Dwork, D. O'Connor, U. Sikora, K. L. Lurie, J. M. Pauly*, et al.*, "Automated, Depth-Resolved Estimation of the Attenuation Coefficient From Optical Coherence Tomography Data," *Ieee Transactions on Medical Imaging,* vol. 34, pp. 2592-2602, Dec 2015.

[79] A. P. Dhawan, R. M. Rangayyan, and R. Gordon, "Image-Restoration by Wiener Deconvolution in Limited-View Computed-Tomography," *Applied Optics,* vol. 24, pp. 4013-4020, 1985.

[80] M. D. Kulkarni, C. W. Thomas, and J. A. Izatt, "Image enhancement in optical coherence tomography using deconvolution," *Electronics Letters,* vol. 33, pp. 1365-1367, Jul 31 1997.

[81] J. M. Schmitt and Z. Liang, "Deconvolution and enhancement of optical coherence tomograms," in *BiOS'97, Part of Photonics West*, 1997, pp. 46-57.

[82] J. L. Starck, E. Pantin, and F. Murtagh, "Deconvolution in astronomy: A review," *Publications of the Astronomical Society of the Pacific,* vol. 114, pp. 1051-1069, Oct 2002.

[83] T. S. Ralston, D. L. Marks, F. Kamalabadi, and S. A. Boppart, "Deconvolution methods for mitigation of transverse blurring in optical coherence tomography," *Ieee Transactions on Image Processing,* vol. 14, pp. 1254-1264, Sep 2005.

[84] Y. H. Liu, Y. M. Liang, G. G. Mu, and X. N. Zhu, "Deconvolution methods for image deblurring in optical coherence tomography," *Journal of the Optical Society of America a-Optics Image Science and Vision,* vol. 26, pp. 72-77, Jan 2009.

[85] M. Balasubramanian and S. Rajaraman, "Retinal and Optic Nerve Head Imaging of Ex Vivo Porcine Eyes using Spectralis SD-OCT," in *Association for Research in Vision and Ophthalmology, Annual Meeting*, Baltimore, MD, 2017.

[86] A. D. Polyanin and A. V. Manzhirov, *Handbook of integral equations*: CRC press, 2008.

[87] D. V. Hinkley, "Inference about the change-point from cumulative sum tests," *Biometrika,* pp. 509-523, 1971.

[88] A. F. Frangi, W. J. Niessen, K. L. Vincken, and M. A. Viergever, "Multiscale vessel enhancement filtering," *Medical Image Computing and Computer-Assisted Intervention - Miccai'98,* vol. 1496, pp. 130-137, 1998.

[89] J. J. Koenderink, "The Structure of Images," *Biological Cybernetics,* vol. 50, pp. 363-370, 1984.

[90] L. M. J. Florack, B. M. T. Romeny, J. J. Koenderink, and M. A. Viergever, "Scale and the Differential Structure of Images," *Image and Vision Computing*, vol. 10, pp. 376-388, Jul-Aug 1992.